Acta Oceanol. Sin., 2020, Vol. 39, No. 7, P. 107–114
https://doi.org/10.1007/s13131-020-1625-x
http://www.hyxb.org.cn
E-mail: hyxbe@263.net

Analysis of the regional spectral properties in northwestern South China Sea based on an empirical orthogonal function

Dongyang Fu[1], Yuye Huang[2, 3*], Dazhao Liu[1], Shan Liao[1], Guo Yu[1], Xiaolong Zhang[1]

[1] College of Electronic and Information Engineering, Guangdong Ocean University, Zhanjiang 524088, China

[2] State Key Laboratory of Tropical Oceanography, South China Sea Institute of Oceanology, Chinese Academy of Sciences, Guangzhou 510301, China

[3] University of Chinese Academy of Sciences, Beijing 100049, China

Received 30 August 2019; accepted 8 October 2019

Abstract

This study presents an analysis of the spectral characteristics of remote sensing reflectance (R_{rs}) in northwestern South China Sea based on the *in situ* optical and water quality data for August 2018. R_{rs} was initially divided into four classes, classes A to D, using the max-classification algorithm, and the spectral properties of whole R_{rs} were characterized using the empirical orthogonal function (EOF) analysis. Subsequently, the dominant factors in each EOF mode were determined.The results indicated that more than 95% of the variances of R_{rs} are partly driven by the back-scattering characteristics of the suspended matter. The initial two EOF modes were well correlated with the total suspended matter and back–scattering coefficient. Furthermore, the first EOF modes of the four classes of R_{rs} (A–D R_{rs}–EOF_1) significantly contributed to the total variances of each R_{rs} class. In addition, the correlation coefficients between the amplitude factors of class A–D R_{rs}–EOF_1 and the variances of the relevant water quality and optical parameters were better than those of the unclassified ones. The spectral shape of class A R_{rs}–EOF_1 was governed by the absorption characteristic of chlorophyll *a* and colored dissolved organic matter (CDOM). The spectral shape of class B R_{rs}–EOF_1 was governed by the absorption characteristic of CDOM since it exhibited a high correlation with the absorption coefficient of CDOM ($a_g(\lambda)$), whereas the spectral shape of class C R_{rs}–EOF_1 was governed by the back-scattering characteristics but not affected by the suspended matter. The spectral shape of class D R_{rs}–EOF_1 exhibited a relatively good correlation with all the water quality parameters, which played a significant role in deciding its spectral shape.

Key words: northwestern South China Sea, remote sensing reflectance, empirical orthogonal function analysis, ocean color control factors

Citation: Fu Dongyang, Huang Yuye, Liu Dazhao, Liao Shan, Yu Guo, Zhang Xiaolong. 2020. Analysis of the regional spectral properties in northwestern South China Sea based on an empirical orthogonal function. Acta Oceanologica Sinica, 39(7): 107–114, doi: 10.1007/s13131-020-1625-x

1 Introduction

One of the foundations of ocean color remote sensing research is the spectral properties of water such as the inherent optical properties (IOPs) and apparent optical properties (AOPs). IOPs depend only on the medium, whereas AOPs depend on the medium, ambient light field, and geometrical distribution (Dickey, 2001). The relations between IOPs and AOPs in a flat homogeneous ocean have been determined from as early as 1975 (i.e., with the remote sensing reflectance (R_{rs}) being proportional to the back-scattering coefficient ($b_b(\lambda)$) and inversely proportional to the absorption coefficient ($a(\lambda)$) (Gordon et al., 1975). Further, a detailed study of the spectral properties of water is extremely essential for developing a regional inverse model, conducting accurate remote sensing monitoring, and strengthening research on the variation of the marine ecological environment. Generally, the R_{rs} spectral variability in a wavelength of 560 nm is used to estimate the total suspended matter (TSM) concentration, and the blue and green parts of the spectrum are used to estimate the chlorophyll *a* (Chl-*a*) concentration. Therefore, the R_{rs} spectral variability in a specific band can be used for monitoring the water quality and developing an inverse algorithm. For example, two R_{rs} band ratio regional algorithms have been applied to the accurate remote sensing estimation of TSM in the Beaufort Sea (Tang et al., 2013). Subsequently, three algorithms (original three-band algorithm, enhanced three-band algorithm, and analytical algorithm) have been employed to retrieve the Chl-*a* concentration in low–level polluted case–II waters, and the enhanced three–band algorithm has been observed to be the most applicable method (Xie et al., 2014).

Empirical orthogonal function (EOF) analysis is useful for analyzing the temporal-spatial variability of marine elements such as that of the phytoplankton pigment concentrations in the

Foundation item: The Key Projects of the Guangdong Education Department under contract No. 2019KZDXM019; the Fund of Southern Marine Science and Engineering Guangdong Laboratory (Zhanjiang) under contract No. ZJW-2019-08; High-Level Marine Discipline Team Project of Guangdong Ocean University under contract No. 002026002009; the Guangdong Graduate Academic Forum Project under contract No.230420003; the "First Class" discipline construction platform project in 2019 of Guangdong Ocean University under contract No. 231419026.

*Corresponding author, E-mail: hyuye0626@163.com

Sea of Japan; here, the remarkable seasonal variations of pigment concentrations and annual pigment blooms appear in spring and fall had been found (Kim et al., 2000). With respect to R_{rs}, classification is an essential method before picturing the spectral variances with wavelengths such as in the study of Ye et al., in which the *in situ* R_{rs} spectra dataset in Yellow Sea was classified into five classes to characterize and investigate the mechanism of the temporal-spatial variability of R_{rs} (Ye et al., 2016). Furthermore, unsupervised hierarchical cluster analysis and EOF analysis were applied to the normalized R_{rs} in the eastern English Channel and southern North Sea, which resulted in the creation of five special distinct classes of R_{rs}; here, 74% of the total variances of R_{rs} could be partly explained by particulate backscattering (Lubac and Loisel, 2007). Therefore, classification and EOF analysis are two good approaches while studying the spectral properties of a certain body of water.

This study aims to analyze and characterize the variances of the spectral properties of water in the northwestern South China Sea, which is often considered to be one of the difficult cases of ocean remote sensing in China owing to the coexistence of case-I and case-II waters. This region is selected mainly because of the complex spectral properties and wide range of variability. The max-classification algorithm is employed to divide the in situ R_{rs} into four classes, namely A–D R_{rs}, and to observe whether different classes of R_{rs} are associated with their water constituents and characteristic properties. Furthermore, EOF analysis is applied to the four classes and entire R_{rs} to provide an assessment of the EOF modes. To determine the main factors dominating the EOF modes, we acquire in conjunction with the water quality and optical measurements, such as the turbidity (TUB), Chl-*a*, TSM, $b_b(\lambda)$, and absorption coefficient of colored dissolved organic matter ($a_g(\lambda)$). The analysis of the spectral properties of water is a primary and necessary step toward monitoring and developing an inverse algorithm for maintaining water quality.

2 Data and methods

2.1 *Study area*

During August 2018, the *in situ* optical and water quality parameters presented in Table 1 were acquired from the northwestern South China Sea (20°–21.5°N, 108.5°–111.0°E), which covers the area of Beibu Gulf, Qiongzhou Strait, and the nearby sea of Leizhou Peninsula. In these regions, strong southwest monsoon in summer and northeast monsoon in winter cause heavy precipitation (Xia et al., 2001). Coastal rivers are the largest discharge source containing abundant nutrient matter, which can be attributed to the establishment of the fourth largest fishery in China in the Beibu Gulf (Liu et al., 1998). High Chl-*a* concentration, strong resuspension and low transparency in these areas can be attributed to the impact of the tide, current, terrestrial source, and aquaculture eutrophication (Huang et al., 2008). The stations sampled during this cruise are shown in Fig. 1, i.e., Stations 1–55. Unfortunately, only 45 of these stations were valid after the exclusion of the abnormal R_{rs}, and Stations of 48–55 were not measured because of the research vessel being broken.

Table 1. Notations used in this study

Parameter	Value
$L_u(\lambda)$	upward radiance (W/m²·sr)
L_{sky}	downward radiance of sky (W/m²·sr)
$E_d(0^+\lambda)$	above sea surface downward irradiance (W/m²·sr)
ρ	Fresnel reflectance of the air–sea interface
λ	wavelength (nm)
R_{rs}	remote sensing reflectance (sr^{-1})
EOF_i	*i*th empirical orthogonal mode
r	Correlation coefficient
Chl-*a*	chlorophyll *a* concentration (μg/L)
TSM	total suspended matter (mg/L)
CDOM	colored dissolved organic matter
$a_g(\lambda)$	absorption coefficient of CDOM
$b_b(\lambda)$	back-scattering coefficient
TUB	turbidity (UTN)

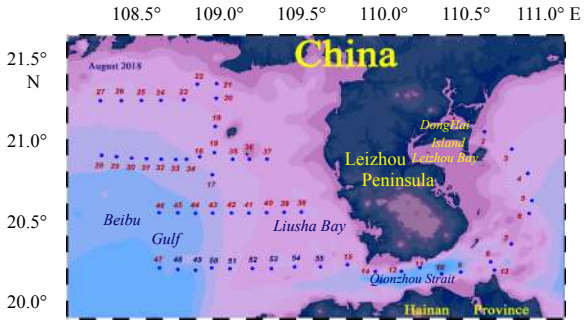

Fig. 1. The study area and the location distribution of different sampling stations in the northwestern South China Sea, including Beibu Gulf, Qiongzhou Strait and the nearby sea of Leizhou Peninsula.

2.2 *Optical parameters and discrete water samples*

Based on the above-water measurement method (Mobley, 1999), hyperspectral radiometric measurements were performed using the TriOS Ramses radiometers. The Fresnel reflectance of the air–sea interface (ρ) was considered to be 0.025 based on the weather. Further, R_{rs} was calculated as

$$R_{rs} = \frac{L_u(\lambda) - L_{sky} \times \rho}{E_d(0^+\lambda)}. \quad (1)$$

The $b_b(\lambda)$ values were obtained based on the average of the *in situ* measurements conducted at a depth of at least 1 m through a HydroScat-6p HS-6 multispectral backscatterer at a field angle of 140°.

The Chl-*a* concentrations were measured using the fluorescence method (GB 17378.7). Here, 2 000 mL samples were initially filtered using 0.47 μm Whatman GF/F filters and stored in a cooler in the dark before being taken back to the laboratory for extraction of 90% acetone for 24 h.

The TSM concentrations were measured via gravimetry (GB 17378.4-2007-27). First, the 2 000 mL water samples were filtered using 0.45 μm membrane filters, dried at 60°C for 24 h, and weighed using a balance with a precision of 1 μg. The weight difference of the filters before and after drying divided by the filtered volume provided the TSM concentrations (Tang et al., 2013).

Accordingly, the $a_g(\lambda)$ values were measured via the spectrophotometery method with the 2 000 mL water samples being filtered using 0.22 μm membrane filters soaked in 10% hydrochloric acid for 15 min prior to filtration, and subsequently kept in a frozen state in dark. Further, the optical density was measured using a UV-2 550 spectrophotometer.

Finally, the turbidity (TUB) was synchronously measured via the RBR maestro multi-parameter water quality monitor.

2.3 *Water type determination algorithm*

As the R_{rs} varies considerably with the water type and presents different optical properties (Allan, 1985), Eq. (2) was developed to divide the waters into case-I and case-II types for a threshold value of 1.5 obtained by $R_{rs}(510)/R_{rs}(412)$. A band ratio of less than 1.5 represents case-I waters; otherwise, it represents case-II waters (Zhang et al., 2005).

$$R_{rs}(510)/R_{rs}(412) = 1.5. \quad (2)$$

2.4 *Classification algorithm of R_{rs}*

The spectral characteristics of R_{rs} change with the water constituents and its concentration, which is observed in case of the six classes of R_{rs} spectral shapes presented in the International Ocean-Colour Coordinating Group (IOCCG) report 3 (IOCCG, 2000). Furthermore, the peak of R_{rs} spectra is, to a large extent, related with the dominant components and its concentrations (Ye et al., 2016), e.g., the peak around 570 nm is considerably related to the concentration of the suspended sediment. Therefore, the max-classification algorithm was developed in this study to classify the R_{rs} into four classes, A–D R_{rs}, as depicted in Fig. 2. The details of each class are provided in the following statements.

Class A: The spectral peak was at 400 nm and exhibited a spectral shape similar to that of type d in the IOCCG report 3 for clear waters.

Class B: Chl-a and CDOM co-dominant waters, with the peak being observed at approximately 490 nm.

Class C: Two or more narrow peaks were presented between 480 and 540 nm in mixed waters with no main dominant components.

Class D: The spectral peak was at approximately 565 nm and dominated by TSM.

2.5 *Empirical orthogonal function analysis*

Alternatively known as an application of the principle component analysis in meteorology, EOF analysis is a type of data decomposition method, i.e, the original dataset is partitioned into

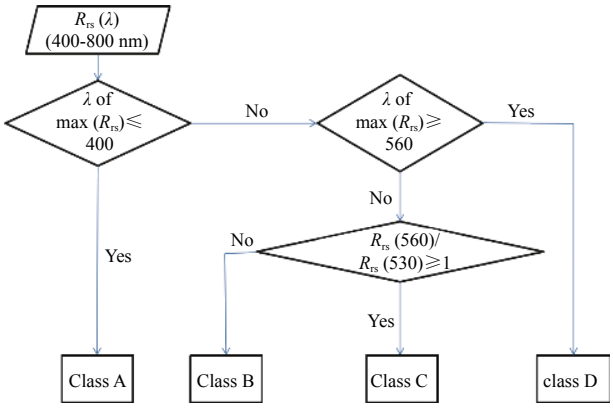

Fig. 2. Flow chart of the maximum classification algorithm. The maximum value of R_{rs} can be used to confirm different classes. The maximum value of classes A, B, and D is at 400, 490, and 565 nm, respectively. However, class C R_{rs} had a wide and flat peak ranging from 480 to 560 nm.

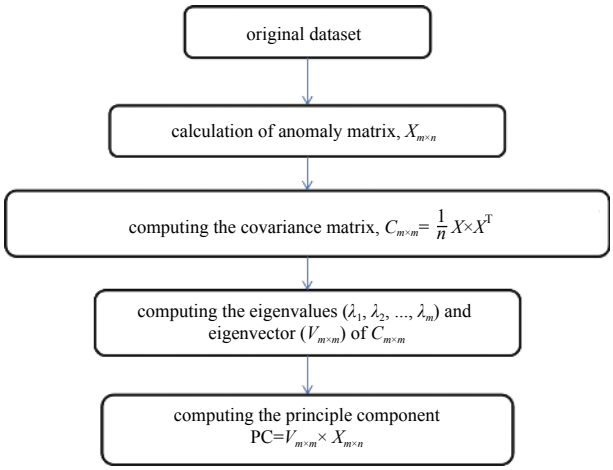

Fig. 3. A flowchart of the EOF analysis process

mathematically orthogonal modes via computation of the eigenvalues and eigenvectors of a spatially weighted anomaly covariance matrix (Ta et al., 2018; Li et al., 2018). The first few orthogonal modes are capable of representing majority of the total variances of the original dataset. The EOF analysis procedure is illustrated in Fig. 3.

In the above Fig. 3, λ_j represents the eigenvalues in descending order, i.e., $\lambda_1 > \lambda_2 > \ldots > \lambda_m$; $V_{m\times m}$ is the eigenvector, and the first column is the first orthogonal mode (EOF_1) corresponding to the first eigenvalue (λ_1); and PC is the principle component corresponding to EOF modes. However, the precision and reliability of these results have to be validated, especially when the field space points exceed the sample capacity. Therefore, a significance test was proposed (North et al., 1982), i.e., calculating the error range ($\Delta\lambda$) of the eigenvalue (λ_j) under a confidence interval of 95% ($\Delta\lambda = \lambda_j\sqrt{\frac{2}{N}}$, with N as the sample capacity) as well as the difference of adjacent eigenvalues ($\lambda_j - \lambda_{j+1}$). Furthermore, the empirical orthogonal mode corresponding to its eigenvalue is considered to be meaningful when the difference between the adjacent eigenvalues is equal or greater than the error range ($\lambda_j - \lambda_{j+1} \geqslant \Delta\lambda$).

3 Results and discussion

3.1 *Water type and ocean color characteristics*

The level of turbidity and water types in the study area are displayed in Fig. 4. Apparently, the spatial distribution of the water types could be characterized based on the coexistence of the case-I and case-II waters. Case-I waters were generally distributed in the offshore area covering the Beibu Gulf and the offshore of Leizhou Bay, whereas case-II waters were located at the Qiongzhou Strait, the Zhanjiang Bay, and the coastal waters around the Leizhou Peninsula (Fu et al., 2015).

Chl-*a* and TSM are two of the three ocean color components, and their distribution and concentrations considerably influence the water spectra. In summer, the spatial variability of Chl-*a* and TSM are similar, with a relatively high concentration being observed in the coastal area that gradually decreases toward the mid-Beibu Gulf, as depicted in Figs 5a and b. Here, the Chl-*a* concentration were 0.6–46 μg/L with a relatively high mean value of 8.03 μg/L. Note that values greater 20 μg/L could be observed outside the Zhanjiang Bay and the center of the Qiongzhou Strait.

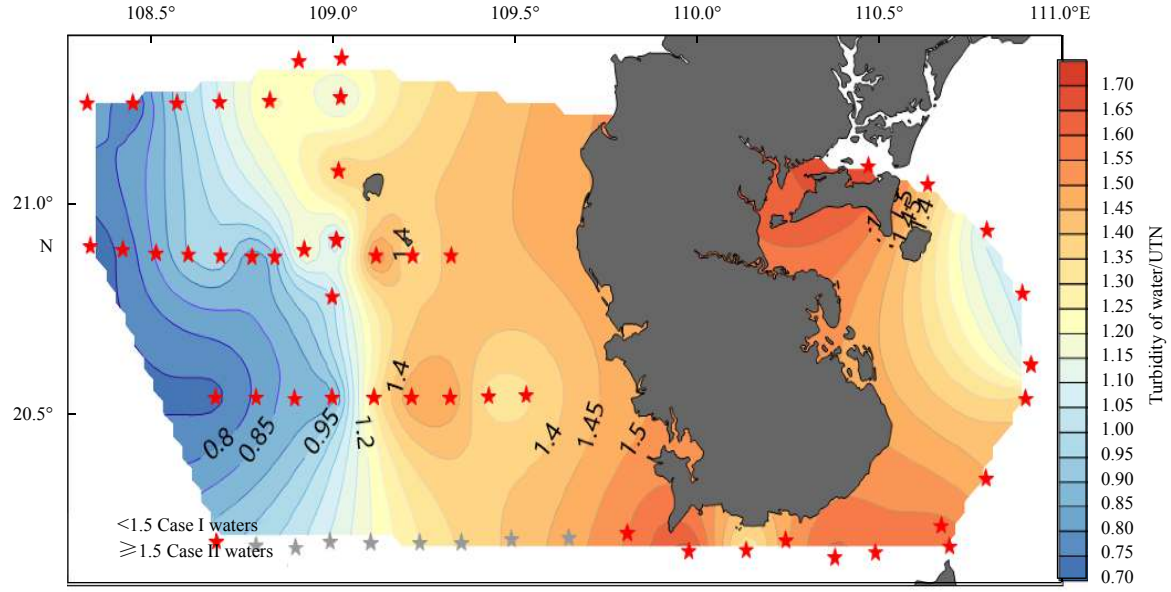

Fig. 4. The level of turbidity and water types in the study area, the color changing from blue to orange shows that the water is increasingly turbid. The value less than 1.5 represents case-I waters; otherwise, it represents case-II waters.

Based on the eutrophication assessment standards using the Chl-*a* concentration from the United States Environmental Protection Agency, these areas contain eutrophic waters. However, in the mid-Beibu Gulf, an oligotrophic water type, the concentration of Chl-*a* is generally low (2 μg/L), except for the surrounding area of the 19th, 37th, 40th and 42nd stations, where it is moderately high in mesotrophic waters.

Further, during summer, a massive amount of fresh water discharge could be observed in the study area through several continental rivers (Xia et al., 2001), which results in the low TSM concentration of 0.2 to 12.2 mg/L and a mean value of 1.89 mg/L. However, the Qiongzhou Strait is a scouring trough with high- and low- velocity currents in the central part and along the coast, respectively. This is the main reason why most of the terrestrial suspended matter flows into the center of the strait and why the highest values of TSM (12.2 mg/L) are found here.

3.2 R_{rs} *variability*

There were considerable differences in the spectral shapes of the *in situ* R_{rs} in the visible domain because of the variance of the water constituents and its concentration, as illustrated in Fig. 6. Regardless, a common spectral shape could be observed, i.e., with the absorption of CDOM and Chl-*a*, the R_{rs} had low values in the blue parts of spectrum. The R_{rs} peak appearing at either 490 or 565 nm was caused by the absorption of CDOM and Chl-*a* and the back-scattering of the suspended sediment, respectively. Additionally, R_{rs} was characterized by a Chl-*a* absorption trough at 670 nm and a fluorescence peak at 680 nm. For wavelengths of longer than 690 nm, R_{rs} was rather low with an increase in pure water absorption (Ye et al., 2016). There was a narrow reflection trough at 760 nm, possibly caused by the strong absorption of water molecules and the low concentration or the absence of the phycocyanin (Ma et al., 2009). In the near-infrared spectrum, R_{rs} was not equal to zero because of the effect of the suspended matter.

3.3 R_{rs} *classification and spectral characteristics*

The mean R_{rs} spectra obtained from each class based on the max-classification algorithm is shown in Fig. 7. Simultaneously, the statistics of in-situ datasets for each class of R_{rs} are shown in table 2. Different classes of R_{rs} demonstrated different spectral shapes as follows.

Class A (N=7): The maximum value of R_{rs} was at 400 nm; regardless, the spectral peak appeared at approximately 490 nm, with R_{rs} gradually decreasing with the wavelength. The near-infrared spectrum R_{rs} was flat and close to zero. Generally, this spectral shape is similar to that of type d in the IOCCG report 3 for clear water. Furthermore, the mean values of water quality and optical measurements were relatively low; however, the mean value of K was particularly high. If K, i.e, the ratio of Chl-*a* to TUB, exhibited a high value, the phytoplankton was considered to be the main particulate matter in this area; otherwise, it represented suspended sediments (Huang et al., 2008). Based on these results, the R_{rs} for this class was mainly distributed in the mid-Beibu Gulf, where phytoplankton was the primary component of the suspended matter and less affected by the terrestrial inputs. These R_{rs} values (all bands) exhibited a high correlation coefficient with $a_g(\lambda)$ ($r > 0.8$), which considerably impacted the spectral properties.

Class B (N=10): A large number of the R_{rs} were measured in the Beibu Gulf, where the turbid level was low. The first peak appeared at approximately 490 nm. Furthermore, the R_{rs} presented low flat values for wavelengths of longer than 600 nm. The mean values of Chl-*a* and $a_g(\lambda)$ (1.82 μg/L and 0.003, respectively) were low, but the change of the spectral shape was influenced by the absorption characteristics of Chl-*a* and CDOM.

Class C (N=13): The R_{rs} for this class were measured near the coast, where the water is slightly turbid. When, compared to the other classes, this class demonstrated three noticeable differences as follows: i) three narrow peaks appeared from 490 to 540 nm; ii) the spectral shape of R_{rs} approximately decreased exponentially from the third peak toward 600 nm; and iii) the fluorescence peak around 680 nm was much stronger with a much higher Chl-*a* concentration when compared with those in classes A and B. The mean values of TSM, b_b (530), and a_g (433) were relatively high (1.98, 0.019, and 0.006 mg/L, respectively). The dominant components of class C were relatively mixed because a de-

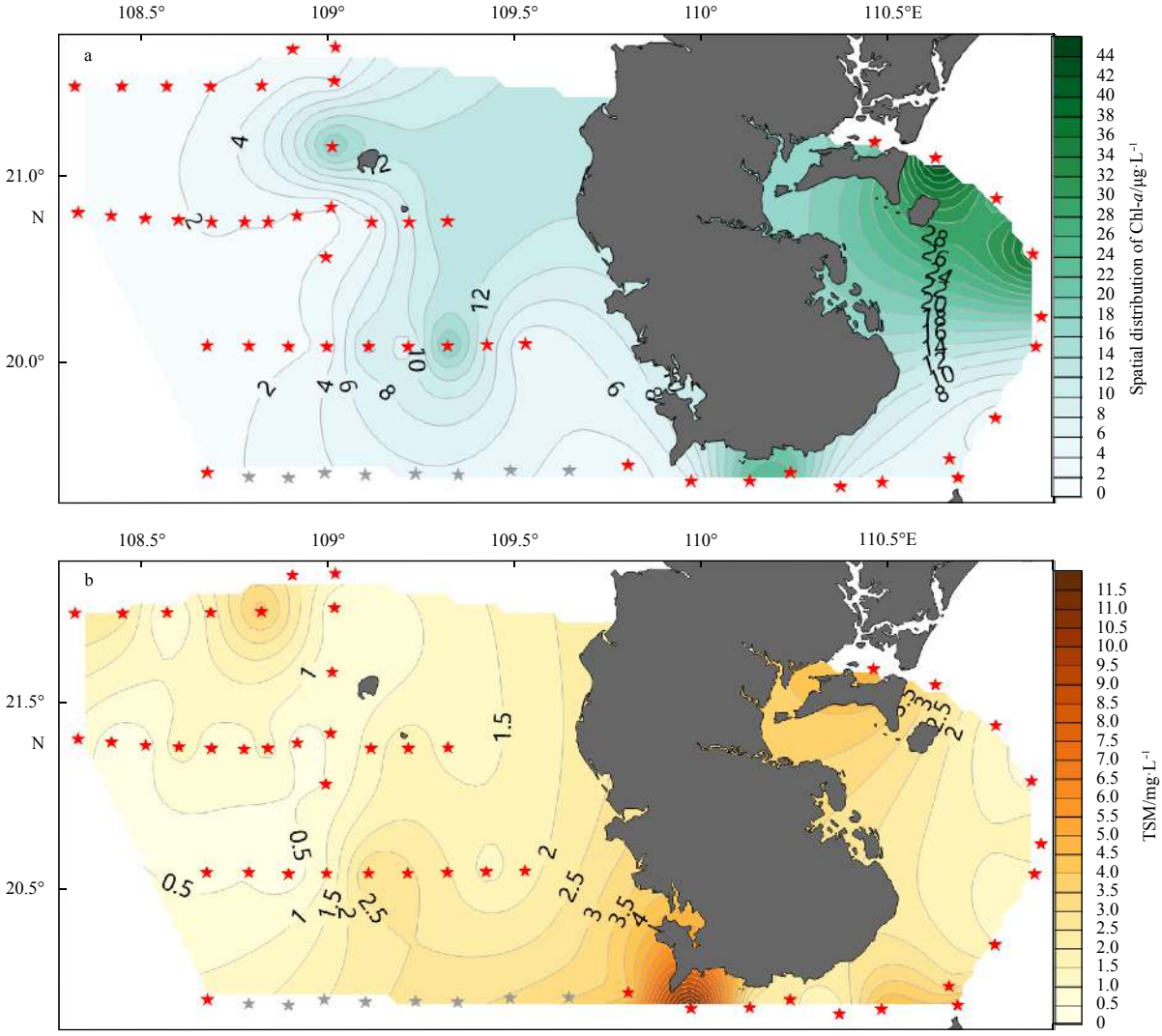

Fig. 5. Spatial distribution of Chl-*a* (μg/L) and TSM (mg/L) in the Beibu Gulf, Qiongzhou Strait and the nearby sea of Leizhou Peninsula in summer. The maximum values of Chl-*a* concentration (46 μg/L) is located at outside the Zhanjiang Bay and the TSM (12 mg/L) is located at the central of the Qiongzhou Strait.

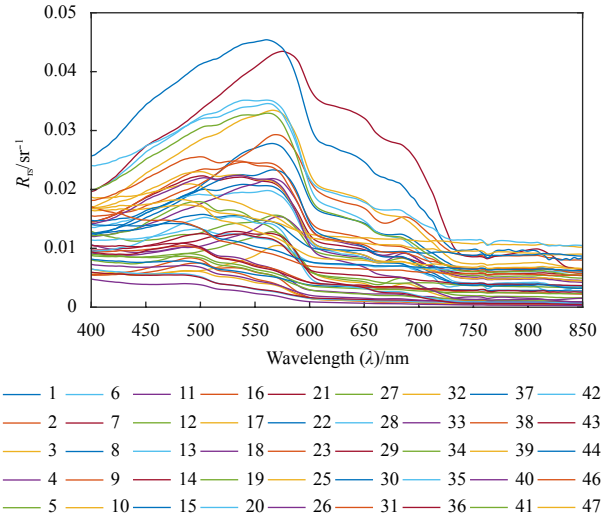

Fig. 6. The whole remote sensing reflectance measured in the northwestern South China Sea in summer (*N*=45).

crease or increase in sediment concentration would transform the class into either class B or class D, respectively.

Class D (*N*=15): Most of the R_{rs} values in this class were measured at the Qiongzhou Strait and the coast of the eastern Leizhou Peninsula. This class differs from the remaining classes because the spectral shape exhibited the strongest back-scattering peak at approximately 565 nm and a significant Chl-*a* fluorescence peak at 680 nm. Additionally, the class had the highest mean concentration yield for TUB, TSM, and Chl-*a* (106.4 UTN, 17.2 mg/L, and 3.08 μg/L, respectively) as measured at 15 stations. Generally, the strong back-scattering of high suspended matter was the primary factor affecting this class.

3.4 *EOF analysis of the whole set of* R_{rs}

Figure 8 shows the first three empirical orthogonal modes of R_{rs} (R_{rs}–EOF_1, EOF_2, EOF_3) based on EOF analysis. The results are reliable because the corresponding differences in adjacent eigenvalues of the first three modes (0.018 1, 0.000 3, and 0.000 5) were considerably greater than the error ranges ($\Delta\lambda$) (0.004 0, 0.000 2, and 0.000 1), which do not overlap. Each EOF mode had its own physical process, i.e., the amplitude factors of each mode varied

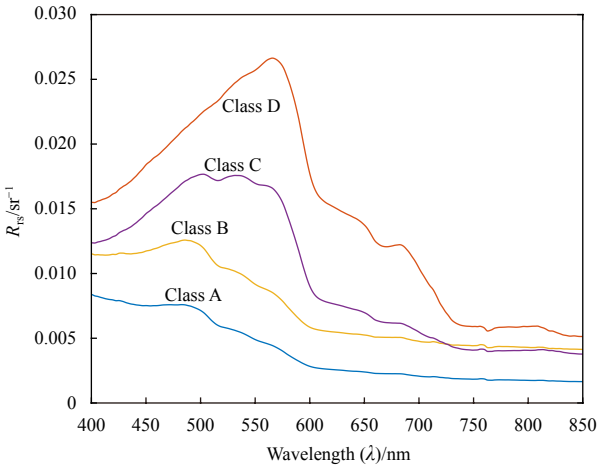

Fig. 7. Spectral shape of the mean R_{rs} obtained for each class.

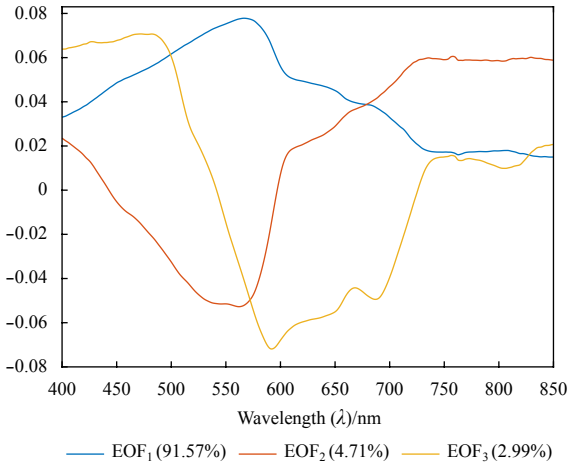

Fig. 8. The first three EOF modes for the whole set of R_{rs}. The first EOF mode (blue curve) accounts for 91.57% of the total variances of R_{rs}, whereas the second and three EOF modes (red and yellow curve) only account for 4.71% and 2.99%, respectively.

with the wavelength. Also, the first three modes explaining 91.57%, 4.71%, and 2.99% of the total variances of the whole R_{rs}, respectively, were more significant than the other modes. Therefore, in this study, only the first three modes were considered.

The positive spectral structure of EOF$_1$ indicates that the variation of the whole R_{rs} was consistent for all the wavelengths. In the blue parts of the spectrum, EOF$_1$ displayed low values, whereas a distinctive back-scattering peak appeared at approximately 565 nm. In addition, EOF$_1$ was characterized by a significant Chl-*a* fluorescence peak usually noticeable around 680 nm. As mentioned above, the spectral structure of EOF$_1$ was extremely similar to that of class D, with a difference of only approximately 0.03 in terms of magnitude. The R_{rs}–EOF$_1$ exhibited a high correlation with TUB (r = 0.50), closely related to the variance of TSM in waters (Kari et al., 2017). TSM and b_b (λ) were also well correlated. Regardless, there was no significant correlation between R_{rs}–EOF$_1$ and Chl-*a* as well as a_g(λ), indicating that the back-scattering characteristics of the suspended particulate matter play an important role on the spectral properties of R_{rs}–EOF$_1$. This result is not surprising because it was previously confirmed by Bertrand and Hubert who found that the first EOF mode of R_{rs} was strongly controlled by the concentration of the back-scattering material as well as the nature of the suspended material (Lubac and Loisel, 2007).

As illustrated in Fig. 8, EOF$_2$ exhibited an almost symmetric spectral shape to EOF$_1$ with a horizontal line of 0.038. In the short-wavelength domain, EOF$_2$ exponentially decreased and exhibited a valley at approximately 565 nm. A weak second positive back-scattering peak appeared at 800 nm. The correlation coefficients between EOF$_2$ and the variance of water quality parameters were almost contrary to those of the EOF$_1$ ones, as depicted in

Table 2. Statistics of in-situ datasets for each class of R_{rs}

Class	Statistics	Chl-*a*	TSM	TUB	a_g(433)	b_b(530)
Class A	min	0.80	0.20	0	0.001	0.002
	max	2.10	2.50	0.33	0.006	0.004
	mean	1.34	1.03	0.11	0.004	0.003
	standard deviation	0.47	0.90	0.35	0.001	0.000
	coefficient variation/%	0.35	0.88	6.85	0.35	0.13
Class B	min	0.60	0.20	0.07	0.002	0.002
	max	2.50	1.40	0.15	0.006	0.004
	mean	1.82	0.73	0.12	0.003	0.005
	standard deviation	0.54	0.43	0.05	0.001	0.007
	coefficient variation/%	0.30	0.59	0.45	0.40	1.40
Class C	min	2.40	0.50	0.00	0.003	0.003
	max	19.4	4.7	165.1	0.025	0.057
	mean	6.78	1.98	39.1	0.006	0.019
	standard deviation	5.75	1.16	68.7	0.006	0.018
	coefficient variation/%	0.85	0.59	1.76	0.96	0.95
Class D	min	3.00	0.80	0.09	0.002	0.012
	max	46.0	12.2	169.5	0.012	0.523
	mean	17.2	3.08	106.4	0.006	0.080
	standard deviation	12.2	2.71	73.7	0.003	0.123
	coefficient variation/%	0.71	0.88	0.69	0.50	15.4

Note: Min and Max represent the minimum and maximum values, respectively. The coefficient variation is the standard deviation divided by the mean.

Figs 9a and b. Furthermore, owing to the good correlation with TUB, b_b (λ), and TSM and coupled with the extremely low correlation with Chl-*a* and a_g (λ), EOF_2 is possibly influenced by the back-scattering characteristics of the suspended particulate matter. The maximum value of EOF_3 appeared at approximately 490 nm, a peak corresponding to some of the *in situ* R_{rs} values. The spectral shape of EOF_3 was driven by the algal suspended particulate matter for ensuring high correlation with Chl-*a* and TUB.

3.5 *EOF analysis of classes A–D* R_{rs}

Figure 10 shows the first empirical orthogonal modes of class A–D, which account for 96.82%, 97.53%, 82.75%, and 92.30% of the total variances, respectively. This study only focused on the description of the first mode (classes A–D R_{rs}–EOF_1) because of this considerable contribution. Further, the correlations between the amplitude factors of classes A–D R_{rs}–EOF_1 and the synchronously measured parameters were better than those of the unclassified ones (Table 3).

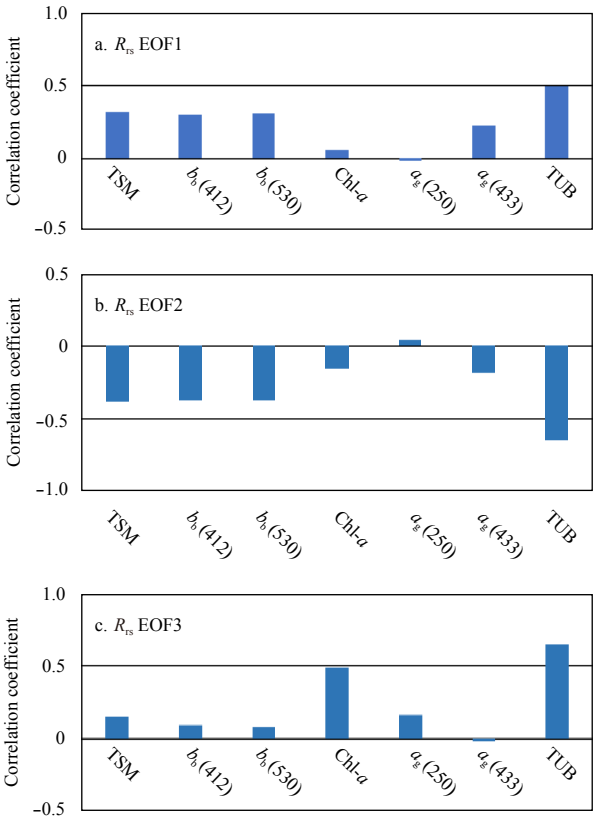

Fig. 9. Correlation coefficient calculated between EOF_i and the discrete in situ water quality and optical parameters. a. EOF_1; b. EOF_2 and c. EOF_3.

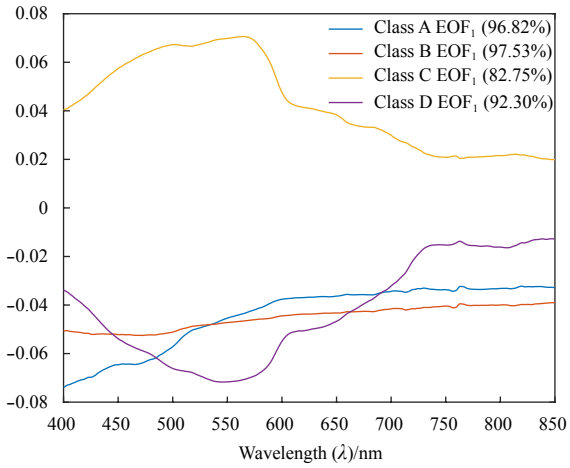

Fig. 10. Spectral shape of the first EOF mode for each class of R_{rs} spectra. Class A EOF_1 (blue curve) accounts for 96.82%, class B EOF_1 (red curve) accounts for 97.53%, class C EOF_1 (yellow curve) accounts for 82.75%, and class D EOF_1 (purple curve) accounts for 92.30%.

Class A R_{rs}–EOF_1 displayed a negative spectral shape in 400–850 nm, which increased with wavelengths up to the near-infrared domain. This R_{rs}–EOF_1 was characterized by a narrow trough at approximately 760 nm and exhibited high correlation coefficients with TSM, Chl-*a*, and a_g (250) (r = –0.94, 0.62, –0.55). indicating that the class A R_{rs}–EOF_1 is driven by the absorption characteristics of Chl-*a* and a_g (λ).

Class B R_{rs}–EOF_1 displayed a negative spectral shape in 400–850 nm similar to a smooth slash and slowly increased with the wavelength. There was only a narrow trough that was observable at 760 nm. This mode was driven by the absorption characteristics of CDOM because a relatively high correlation was observed with a_g (433) (r = –0.40). The relation of the R_{rs}–EOF_1 with TSM was good.

Class C R_{rs}–EOF_1 displayed a positive spectral structure in 400–850 nm and rapidly increased between the blue and green parts of the spectrum. The first peak appeared at approximately 490 nm, with the maximum peak appearing at approximately 560 nm. This class was also characterized by a weak second back-scattering peak of suspended sediment at approximately 810 nm. Its high correlation with b_b (412) (r = –0.60) denoted that it was influenced by the back-scattering characteristics that were not caused by the suspended matter owing to the low relation with the TSM. Furthermore, its relation with a_g(433) was not very bad (r = 0.48); therefore, the absorption characteristics of CDOM also exhibited weak influence on this mode.

Coincidentally, the spectral shape in case of class D R_{rs}–EOF_1

Table 3. The correlation coefficient calculated between the classes A–D R_{rs}–EOF_1 and the variance of optical and water quality parameters

Correlation coefficient	Class A EOF_1	Class B EOF_1	Class C EOF_1	Class D EOF_1
TSM	–0.94	0.47	–0.02	0.49
b_b(530)	–0.39	0.07	–0.53	0.44
b_b(412)	–0.45	0.07	–0.60	0.47
Chl-*a*	0.62	0.06	–0.12	–0.51
a_g(250)	–0.55	0.13	0.38	–0.30
a_g(433)	–0.49	–0.40	0.48	–0.44
TUB	–0.18	0.29	0.33	–0.59

was contrary to that of the class D R_{rs}, e.g., a R_{rs}–EOF_1 valley appeared at approximately 565 nm, and the R_{rs} of class D showed a reflection peak (Fig. 7). This class showed a relatively good correlation with all the synchronously measured parameters (r was approximately 0.5). Furthermore, the class D R_{rs}–EOF_1 spectrum seemed to be affected by the absorption and back-scattering characteristics of multiple water quality parameters.

4 Conclusions

In this study, the max-classification algorithm and EOF analysis were applied to analyze the spectral properties of R_{rs}. Further, the relations between each EOF mode and the synchronously measured parameters were discussed. The results demonstrated that different EOF modes exhibit different dominant factors. The first two orthogonal modes of the whole R_{rs} were driven by the back-scattering characteristics of the suspended particulate matter. Meanwhile, the correlations between the classes A–D R_{rs}–EOF_1 and the variances of the relevant water quality and optical parameters were better than those in the unclassified ones; therefore, it became easier to identify the dominant factors. Furthermore, since different dominant factors of EOF_i can be converted into the homologous dominant factors of R_{rs}, the results validated the effectiveness of the max-classification algorithm and EOF analysis for analyzing the spectral characteristic of R_{rs}. Finally, because EOF is a type of data decomposition method, this study presented an important experiment for analyzing a bigger dataset in the future.

References

Allan T D. 1985. Remote assessment of ocean color for interpretation of satellite visible imagery: In Gordon H R and Morel A Y, eds. Lecture Notes on Coastal and Estuarine Studies. Berlin: Springer-Verlag, 114.

Dickey T D. 2001. Inherent optical properties and irradiance. In: Steele J H, ed. Encyclopedia of Ocean Sciences. Oxford, UK: Academic Press, 244–253

Fu Dongyang, Zhang Ying, Liu Dazhao, et al. 2015. Evaluation model of coastal water quality and application research based on principal component analysis—a case of Leizhou Peninsula waters. Journal of Marine Sciences (in Chinese), 33(1): 45–50

Gordon H R, Brown O B, Jacobs M M. 1975. Computed relationships between the inherent and apparent optical properties of a flat homogeneous ocean. Applied Optics, 14(2): 417–427, doi: 10.1364/AO.14.000417

Huang Yichen, Li Yan, Shao Hao, et al. 2008. Seasonal variations of sea surface temperature, chlorophyll-a and turbidity in Beibu gulf, MODIS imagery study. Journal of Xiamen University (Natural Science) (in Chinese), 47(6): 856–863

IOCCG. 2000. Remote sensing of ocean colour in coastal, and other optically-complex, waters. Dartmouth, Canada: IOCCG

Kari E, Kratzer S, Beltrán-Abaunza J M, et al. 2017. Retrieval of suspended particulate matter from turbidity–model development, validation, and application to MERIS data over the Baltic Sea. International Journal of Remote Sensing, 38(7): 1983–2003, doi: 10.1080/01431161.2016.1230289

Kim S W, Saitoh S I, Ishizaka J, et al. 2000. Temporal and spatial variability of phytoplankton pigment concentrations in the Japan Sea derived from CZCS images. Journal of Oceanography, 56(5): 527–538, doi: 10.1023/A:1011148910779

Li Qinzheng, Chen Peng, Sun Langlang, et al. 2018. A global weighted mean temperature model based on empirical orthogonal function analysis. Advances in Space Research, 61(6): 1398–1411, doi: 10.1016/j.asr.2017.12.031

Liu Zilin, Ning Xiuren, Cai Yuming. 1998. Distribution characteristics of size-fractionated chlorophyll a and productivity of phytoplankton in the Beibu Gulf. Haiyang Xuebao (in Chinese), 20(1): 50–57

Lubac B, Loisel H. 2007. Variability and classification of remote sensing reflectance spectra in the eastern English Channel and southern North Sea. Remote Sensing of Environment, 110(1): 45–58, doi: 10.1016/j.rse.2007.02.012

Ma Ronghua, Kong Weijuan, Duan Hongtao, et al. 2009. Quantitative estimation of phycocyanin concentration using MODIS imagery during the period of cyanobacterial blooming in Taihu Lake. China Environmental Science (in Chinese), 29(3): 254–260

Mobley C D. 1999. Estimation of the remote-sensing reflectance from above-surface measurements. Applied Optics, 38(36): 7442–7455, doi: 10.1364/AO.38.007442

North G R, Bell T L, Cahalan R F, et al. 1982. Sampling errors in the estimation of empirical orthogonal functions. Monthly Weather Review, 110(7): 699–706, doi: 10.1175/1520-0493(1982)110<0699:SEITEO>2.0.CO;2

Ta Zhijie, Yu Ruide, Chen Xi, et al. 2018. Analysis of the spatio-temporal patterns of dry and wet conditions in central Asia. Atmosphere, 9(1): 7, doi: 10.3390/atmos9010007

Tang Shilin, Larouche P, Niemi A, et al. 2013. Regional algorithms for remote-sensing estimates of total suspended matter in the Beaufort Sea. International Journal of Remote Sensing, 34(19): 6562–6576, doi: 10.1080/01431161.2013.804222

Xia Huayong, Li Shuhua, Shi Maochong. 2001. Three-D numerical simulation of wind-driven current and density current in the Beibu Gulf. Acta Oceanologica Sinica, 20(4): 455–472

Xie Fei, Guo Ziqi, Tian Ye, et al. 2014. The preliminary inquiry of Chlorophyll-a inversion algorihtms applicable to guanting reservoir. In: Proceedings of 2013 IEEE International Geoscience and Remote Sensing Symposium. Melbourne, VIC, Australia: IEEE, 3785–3788, doi: 10.1109/IGARSS.2013.6723655

Ye Huping, Li Junsheng, Li Tongji, et al. 2016. Spectral classification of the Yellow Sea and implications for coastal ocean color remote sensing. Remote Sensing, 8(4): 321, doi: 10.3390/rs8040321

Zhang Tinglu, Shi Yingni. 2005. A method to classify case I and case II waters. Periodical of Ocean University of China (in Chinese), 35(5): 849–853